Effect of Aromatic Sulfonate Ligand on the Photovoltaic Performance of Molybdenum Cluster-Sensitized Solar Cell

Thi Kim Ngan Nguyen[1,*], Satoshi Ishii[2], Adèle Renaud[3], Fabien Grasset[3,4], Stéphane Cordier[3], Noée Dumait[3], Hiroshi Fudouzi[5], Tetsuo Uchikoshi[4,5]

[1] International Center for Young Scientists, Global Networking Division, National Institute for Materials Science, 1-2-1 Sengen, Tsukuba, Ibaraki 305-0044, Japan

[2]Research Center for Materials Nanoarchitectonics (MANA), National Institute for Materials Science, 1-1 Namiki, Tsukuba, Ibaraki 305-0044, Japan

[3]Univ. Rennes-CNRS-Institut des Sciences Chimiques de Rennes, UMR6226, 35000 Rennes, France

[4]CNRS–Saint-Gobain–NIMS, IRL3629, Laboratory for Innovative Key Materials and Structures, National Institute for Materials Science, 1-1 Namiki, Tsukuba, Ibaraki 305-0044, Japan

[5]Research Center for Electronic and Optical Materials, National Institute for Materials Science, 1-2-1 Sengen, Tsukuba, Ibaraki 305-0044, Japan

Corresponding author: Thi Kim Ngan NGUYEN

Full postal address: National Institute for Materials Science (NIMS), 1-2-1 Sengen, Tsukuba, Ibaraki 305-0047, Japan

E-Mail address: NGUYEN.Thikimngan@nims.go.jp

Abstract

The photovoltaic performance of molybdenum cluster-sensitized solar cells (MCSSCs) has been explored with the challenge of enhancing their efficiency due to the low charge transfer efficiency. Aromatic sulfonate ligands (NS = naphthalene 2,6-disulfonate = $^{-}OSO_2$-$C_{10}H_6$-SO_3^{-}) were now used for the functionalization of the $\{Mo_6I^i_8\}$ cluster cores. The new functional $[Mo_6I^i_8I^a_3(H_2O)^a_2(NS^{-}Na^{+})^a]$ cluster unit exhibits enhanced photophysical and photoelectrochemical properties compared to other homologues based on the $\{Mo_6I^i_8\}$ cluster cores. In greater detail, the role of the NS functional groups was beneficially emphasized for the improved oxidation stability of the cluster in a redox mediator, adjusting of the emission lifetime to a suitable range for fast electron injection, and accelerating the charge transport process. The best as-synthesized Mo_6 cluster-based solar cell resulted in a stable photocurrent of 2.38 $mA.cm^{-2}$ with a fill factor of 0.63 and the power conversion efficiency of 0.97%

under AM 1.5 illumination, a 2 times enhancement in comparison to the reference iodide Mo_6 cluster-based cell (0.52 %). Specific attention focused on the increase of the power conversion efficiency up to 1.18 % after 330 seconds, then reached the saturation trend. The enhanced charge transfer of the metal cluster complex was obtained from facile modifications of the functional apical ligands that result in advantageous photophysical and electrochemical characteristics specializing in optoelectronic devices. This study provides the general methodology and knowledge for the next improvement of the photovoltaic efficiency of the Mo_6 cluster-based sensitized solar cells.

Keywords: molybdenum cluster, optoelectronic, charge transfer, solar cell, photoluminescent lifetime.

1. Introduction

With attention to reducing fossil fuels in energy production, scientists are now evaluating new materials and technologies for converting solar light energy into electricity [1]. The high cost of manufacturing and raw materials of Si-based solar technology leads to the exploration of third-generation photovoltaic devices with emerging solar cells based on low-cost and abundant materials, ease of shaping, and flexible design. This photovoltaic generation involves various technologies, such as organic, perovskite, or organic–inorganic hybrid perovskite solar cells, differing by the nature of the photoelectrode materials [2-4]. Dye-sensitized solar cells (DSSCs), quantum dot-sensitized solar cells (QDSSCs), and metal cluster-sensitized solar cells (MCSSCs) are based on the same design. They contained two electrodes, a photoanode based on the transparent semiconductor layers recovered by molecular light-harvesters, i.e. organic dyes, quantum dots, or metal clusters, and a metallic counter electrode, separated by an electrolyte composed of a redox mediator. The emergence of light-harvester-sensitized solar cells was developed by Grätzel and his colleagues in 1991, resulting in an impressive power conversing efficiency (PCE) of 7.9 % [5]. Since then, many studies based on the development of 0-3D nanostructured semiconductors, photosensitizers, counter electrodes, redox electrolytes, and device architectures have allowed improving the energy conversion efficiency of the DSSCs [6-8]. The best photovoltaic performance (η %) of DSSCs recently reported 15.2 % under 1.5 global simulated sunlight, while it is 15.31 % recorded for QDSSCs [9-10].

In the dynamics of exploring new potential sensitizers, metal atom clusters were introduced as light-harvesting materials in the MCSSCs. The Au, Pt, Pd, and Ag-based metal clusters have been investigated which led to the overall efficiencies of 2.4 % for thiolate gold, 1.1 % for silver-copper

nanoalloy, and 0.26 % for $Ag_{16}(SG)_9$ nanoclusters [11-13]. However, the limitation of MCSSCs based on these metal clusters was a lower absorption in the visible range. The photosensitizer plays an important role since it absorbs the light energy for supplying photo-excited electrons to generate the photocurrent. Therefore, many efforts have been made to strengthen the function of the sensitizers such as i) absorption in the visible light range, ii) the quenching of the photoexcited electron, iii) the stabilization and regeneration of sensitizer in the redox mediator, and iv) the beneficial electron transfer and electron lifetime in the redox electrolyte [14-17].

A metal cluster family with a unique electron structure has been introduced as a broadly visible light absorber. The face-capped $[(Mo_6X^i_8)L^a_6]^{-2}$ cluster (X^i = halogen, L^a = halogen, functional groups, H_2O, etc.) was built on an octahedral Mo_6 cluster that bonded with 8 inner ligands in face-capping positions and 6 apical ligands in terminal positions [18-20]. The charge of the negatively charged cluster was balanced by inorganic or organic counter-cations (e.g.; alkali cation or quaternary ammonium) [21-22]. The nanosized Mo_6 cluster appeared attractive as a photosensitizer due to its high photostability, large Stoke shift for reducing the absorbing energy, and feasible modification of the chemical composition for adjusting the optical bandgap [18, 23]. The Mo_6 cluster was able to create a photoexcited electron under visible light irradiation, however, the material itself limited charge transfer for optoelectronic applications. For this reason, the incorporation of the Mo_6 cluster with a semiconductor has essentially been studied to enhance the charge transfer via covalent bonds or ionic interactions. Several designs have been studied using TiO_2 for solar cells, double layer hydroxides or tin pyrophosphate semiconductors for photoconductivity sensors, and graphene oxide for enhanced photoinactivation [18, 24-26].

Recently, a general study revealed the photovoltaic efficiency of the Mo_6 cluster as an absorber in n and p-type solar cells prepared by using an electrophoretic deposition process (EPD), resulting in the best performance efficiency of 0.44 % [18-19, 27]. The lack of knowledge about the photophysical and photoelectrochemical behaviors of the Mo_6 cluster in the redox mediator of MCSSCs inspired the investigation of the study. According to the Shockley-Queisser (SQ) limitation for a single p-n junction, the optimal band gap (E_g) of the absorber is situated around 1.3 eV [28]. In a previous study, the band gap of the Mo_6 cluster iodides was measured at 1.9 eV and it is stable when iodide apical ligands of the $Cs_2[\{Mo_6I^i_8\}I^a_6]$ precursor were replaced by several water molecules to form the $[Mo_6I^i_8I^a_4(H_2O)^a_2].x\ H_2O$ cluster [19, 24, 27]. By integrating such Mo_6 clusters as sensitizers in n- and p-type MSSCs, a proof of concept was obtained. Such molecular clusters can be used as light harvesters to

photoinduce both electron and hole transfers. The ambipolar behavior of such Mo_6-based layers was more recently demonstrated [27]. However, with a short-circuit (J_{sc}) current of 1.13 mA.cm^{-2} and an open circuit (V_{oc}) of 529 mV, the recorded performances were low [19]. They were attributed to a non-effective charge transfer. The iodide Mo_6 cluster had a weak photoluminescence, however, its emission lifetime was beneficially revealed in the microsecond range [20]. The photophysical properties, absorbance, and photoluminescence could be modified by the nature of the inner and/or apical ligands and affected by the number of valent electrons in a cluster unit [20]. This study confirmed a relative relation between the chemical composition of the apical ligands of the cluster and the emission lifetime. A photosensitizer should be luminescent with a favorably long emission lifetime in a range between μs and ns, being faster than the process of charge injection (0.1 ns) [2]. With the emission lifetime in the microsecond range, the photoexcited electrons on the Mo_6 cluster are able to be injected into the conduction band of the semiconductor electrode in the MCSSCs. Although the Mo_6 clusters do not have an optimal absorption in the visible range when compared to porphyrin; for example, a broad absorbing spectrum, limited self-quenching of the excited state at a high concentration and low photobleaching it can compensate for these drawbacks [29].

Under these circumstances, the goal of this study is to introduce functional groups at the terminal positions of the Mo_6 cluster for i) improving the interactions of the Mo_6-based sensitizer with the semiconductor substrate, ii) improving the efficiency of electron injection by adjusting the emission lifetime of the photoexcited electrons in the suitable range, and iii) limiting the aggregation of adsorbed clusters which can quench the photoexcited electron. Starting from the Mo_6 cluster iodide precursor $Cs_2[\{Mo_6I^i_8\}I^a_6]$, a few iodide ligands were replaced by naphthalene 2,6-disulfonate (NS) organic molecules, composed of electron-donating naphthalene and electron-withdrawing sulfonate for delocalizing the photoinduced electron. An X-ray photoelectron analysis confirmed the chemical compositions of the as-synthesized compounds including the $[Mo_6I^i_8I^a_3(H_2O)^a_2(\text{-}OSO_2\text{-}C_{10}H_6\text{-}SO_3^-Na^+)^a]$ clusters and free $Na_2(\text{-}OSO_2\text{-}C_{10}H_6\text{-}SO_3^-)$ molecules with different constitutions that depended on the molar ratios of the $Cs_2[\{Mo_6I^i_8\}I^a_6]$ precursor and NS. The replacement of iodide ligands by NS molecules resulted in modification of the band gaps with the shift from 2.08 eV to 2.60 eV and increased the radiative recombination rate that was indicated by a broad peak centered around 640 nm in the photoluminescence spectra. The radiative recombination time of the modified Mo_6 cluster was adjusted in the suitable range (ns < τ < μs) for photovoltaic cells, the longer than electron injection

time (~ 0.1 ns), and shorter than the cluster regeneration time (~ 0.1 μs) in the electrolyte mediator [2]. The photovoltaic properties were systematically studied to reveal the role of NS at different compositions on isolated and non-isolated Mo_6 cluster-based nanocomposites. Both the $[Mo_6I^i_8I^a_3(H_2O)^a_2(\text{-}OSO_2\text{-}C_{10}H_6\text{-}SO_3^-\ Na^+)^a]$ clusters and free $Na_2(\text{-}OSO_2\text{-}C_{10}H_6\text{-}SO_3^-)$ molecules contributed to the enhancement of the homogeneous dispersion of the Mo_6 cluster and charge transferring rate such that the power conversion efficiency (PCE = 0.97 %) increased by a factor of 2 compared to a previous study (0.44 %) [19]. This is a new record of efficiency for Mo_6-based cluster-sensitized solar cells. The Mo_6 cluster-based cells resulted in an impressive accumulation of the photocurrent while the NS at a good concentration can retain the enhanced photocurrent in the MINS-based cells. With regard to this, an increase in PCE by about 20 % after the first 5 minutes of the AM 1.5G illumination was recorded until it reached saturation. These promising results open the door for the investigation of the octahedral transition metal clusters as a new nontoxic light harvester for photoelectrochemical devices ranging from sensitizer solar cells to solid solar cells.

2. Experimental sections

Chemicals

Acetone (99.5 %) and acetonitrile were supplied from Nacalai Tesque. The titanium chloride solution ($TiCl_4$, 16.0～17.0 % as Ti) and disodium naphthalene-2,6-disulfonate were purchased from the Fujifilm Wako Pure Chemical Collaboration. Ti-Nanoxide T/SP, which contains anatase titanium dioxide particles with a size of about 15-20 nm and a concentration of 18 wt%, was purchased from Solaronix. The compositions of the electrolytes that included I_2, LiI,1-butyl-3-methylimidazolium iodide, and (2) 4-tertbutylpyridine were purchased from Sigma-Aldrich. All the chemicals were used without purification. The deionized water was obtained using Water Purifiers WG710 equipment with conductance of 0.5×10^{-4} S/m at 25°C. The $Cs_2[\{Mo_6I^i_8\}I^a_6]$ (CMI) cluster powder was synthesized by the solid-state procedure reported in a previous publication without purification [30].

Modification of apical ligand of $Cs_2[\{Mo_6I^i_8\}I^a_6]$ (CMI) cluster

The $Cs_2[\{Mo_6I^i_8\}I^a_6]$ (CMI) cluster precursor was dissolved in acetone (1 g/L) and the naphthalene 2,6-disulfonate (NS) organic molecule was separately dissolved in distilled water at room temperature under ambient conditions. The molar ratios are listed in Table SI1. Both solutions were then mixed at 70°C for 3 hours and continually stirred at room temperature for 48 hours. The transparent and red-

colored solution containing CMI shifted to a slightly turbid orange. The slurries were abbreviated as non-isolated MINSx with x=16, 24, and 35, and x as an abbreviated representation of the molar ratios between NS and the CMI precursors. (**Tab. S1**). In addition, all the MINSx slurries were purified by washing four times in an acetone/water mixture to remove any residual substances, then heated at 50^{o}C for 24 hours, and abbreviated as isolated MINSx with x=16, 24, and 35. All the prepared composites were stored at 50^{o}C for the next steps and deposited on quartz glass for characterization.

Preparation of the Mo_6 cluster-based photoelectrodes

The mesoporous titanium dioxide (TiO_2) film was prepared on a highly durable transparent conductive ITO glass (Geomatec Co., Ltd., Tokyo, Japan; < 5 Ohm/sq). the 2×3 cm^2 ITO glass was first properly washed using acetone and ethanol, then coated with a commercial Ti-Nanoxide paste by the doctor blade technique with a thickness of about 5µm. Afterward, the TiO_2 paste-based photoelectrode was sintered at 450 °C for 1 hour in ambient air to decompose the unnecessary organic compositions, then cooled to room temperature. A titanium (IV) chloride surface ($TiCl_4$) treatment was performed on the mesoporous TiO_2 film that was referenced from a previous procedure to enhance the charge transport [31]. The electrodes were immersed in a $TiCl_4$ solution (0.3 M) of distilled water at 70 °C for 30 min. The electrode was then washed using distilled water to remove the white TiO_2 nanoparticles on the surface, then sintered at 450 °C for 30 min in ambient air. The active TiO_2 area for the absorbing photosensitizer was 1.2×1.5 cm^2. The non-isolated $MINS_x$ (x=16, 24, 35) suspensions were directly poured into a 500 mL beaker and stabilized in a vacuum impregnation apparatus. The $TiCl_4$-treated TiO_2 mesoporous film was immersed in the photosensitizer-containing beaker for 15 minutes under vacuum pressure (~ 6 Pa). The photoelectrode was then heated at 120 °C for 30 minutes to properly eliminate the solvent and perform possible covalent bonding between the TiO_2 and Mo_6 cluster-based photosensitizer. A negative MI nanocluster was also deposited on the TiO_2 electrode by electrophoretic deposition (EPD) at 20 V for 2 minutes as in the illustration below. The EPD system consisted of one indium tin oxide-coated glass slide with a surface area of 2×3 cm^2 acting as the cathode and one $TiCl_4$-treated TiO_2 mesoporous film acting as an anode that was connected to a Source Meter (Keithley Model 2400, Ohio, USA) as an electric field generator. All the TiO_2 photoelectrodes adsorbed Mo_6 cluster-based photosensitizers were stored at 50 °C before characterization.

Solar cell fabrication

The n-MCSSCs were an assembled structure of two photoelectrodes with filtered electrolytes in the middle space. A counter electrode was prepared by quickly coating a platinum layer at a current of 5 mA for 5 minutes under plasma treatment. The $TiCl_4$-treated TiO_2 photoanode coated with photosensitizers was sealed with a platinum-coated ITO glass using a Surlyn polymer spacer (Meltonix 1170-25, 25 µm) at 120 °C for 10 minutes. The electrolyte composed of the iodide/triiodide couple was referenced from the previous report with a slight modification for comparison [19]. The redox mediator compositions included 0.05 M I_2, 0.1 M LiI, 0.6 M 1-butyl-3-methylimidazolium iodide, and 0.5 M (2)4-tertbutylpyridine in acetonitrile. The J-V characteristic was recorded by a Keithley 2400 source meter under the illumination of one sun (AM 1.5G illumination, HAL-320, Asahi Spectra USA, Inc.) with a power density of 100 $mW.cm^{-2}$.

The overall efficiency (PCE, %) is the percentage of the solar energy converted into electrical energy under the illumination of one sun calculated using equation (1) [2]:

$$\eta\ (\%) = \frac{J_{sc} \times V_{oc} \times FF}{P_{in}} \quad (1)$$

where J_{sc} is the current per active area recorded using a source meter (2400, Keithley) under the illumination of one sun (AM 1.5G illumination) with a P_{in} of 100 $mW.cm^{-2}$. V_{oc} and FF are the open circuit voltage and fill factor, respectively.

The incident photon-to-current conversion efficiency (IPCE) of the n-MCCSC was calculated using equation (2) [2]:

$$\text{IPCE} = \frac{J_{sc} \times 1240}{P_{in} \times \lambda} \quad (2)$$

where J_{sc} is the photocurrent per active area recorded using a source meter (2400, Keithley) under the illumination of a wavelength-tunable light source (NIJI-2, Bunkoukeiki) with P_{in} (mW/cm^2), and λ is the corresponding excitation wavelength.

Material characterizations

The binding energy spectra were measured by X-ray photoelectron spectroscopy (XPS) (PHI Quantera SXM (ULVAC-PHI)) using Al Kα radiation at 20 kV and 5 mA and the binding energies were calibrated with the C1s peak at 285 eV. The typical chemical vibrations were verified by Raman spectroscopy (RAMAN plus, Nanophoton Co., Ltd., Japan) in the wavenumber range from 0 to 1800 cm^{-1} under the excitation of the laser wavelength of 532 nm and Fourier transform infrared spectroscopy (FTIR) (Thermo Scientific Nicolet 4700) in the wavenumber range from 4000 to 400

cm^{-1}. The crystallinity of the mesoscopic TiO_2 photoelectrode was determined by powder X-ray diffraction (XRD) (SmartLab, RIGAKU, 40 kV and 30 mA) in the 2θ angle range from 20° to 60° for the thin film at the scan speed of 1°/ min with the Cu Kα radiation (λ = 1.54 Å). The absorbance properties were measured by UV-Vis-NIR spectroscopy (JASCO V-650, Jasco Corp.) in the wavelength range of 350 to 1000 nm at the scan rate of 1000 nm/min. The absorbance spectra were used to calculate the optical bandgap (E_g) by using the Tauc relation as demonstrated in the Support Information. The emission spectra were obtained by high-performance fluorescence spectroscopy (JASCO FP8500) connected to a Xenon lamp at the scan rate of 500 nm/min. The surface morphology and the elemental composition were analyzed by field emission scanning electron microscopy (FE-SEM, S4800, Hitachi High-Technologies Corp.) at 10 kV coupled with an energy-dispersive X-ray (EDX) analysis device. The quantum yield was measured by an absolute PL quantum yield spectrometer C11347 (Hamamatsu Corp.) with excitation at a wavelength of 400 nm. Time-resolved photoluminescence (TRPL) signals were recorded via Time-Correlated Single Photon Counting (TCSPC) using HORIBA Scientific fluorescence lifetime systems coupled with a pulsed diode laser (NanoLED-360, Horiba) to excite the samples at the wavelength of 361 nm, pulse duration lower than 1 ns, and time-to-amplitude converter (TAC) of 2 ms in an air atmosphere at 298 K.

Cyclic voltammetry

The cyclic voltammetry experiments were carried out in a three-electrode cell including a platinum plate (1 cm^2) as the working electrode, a platinum wire as the counter electrode, and a saturated silver/silver chloride (Ag/AgCl) in 3.5 M KCl as the reference electrode. The Mo_6 cluster prepared by EPD and isolated MINS24 compounds were separately dissolved in acetonitrile at 1 mM, then mixed with the $TEABF_4$ 0.1M supporting electrolyte. The ferrocene/ferrocenium redox system was used as an internal system to calibrate the E^{ox} and E^{red} calculations. The estimated highest occupied molecular orbital (HOMO) and lowest unoccupied molecular orbital (LUMO) energies of the photosensitizers were calculated using the equation: $E_{LUMO} = -e[(E_{red} - E_{1/2(ferrocene)} + 4.8)$ eV or $E_{HOMO} = -e[(E_{ox} - E_{1/2(ferrocene)} + 4.8)$ including the ferrocene reference energy level of - 4.8 eV [32]. The half-wave potential $E_{1/2(ferrocene)}$ of the ferrocene/ferrocenium (Fc/Fc^+) redox couple in acetonitrile with the $TEABF_4$ 0.1M supporting electrolyte was found to be 0.448 V (Supporting Information). The solution was degassed by purging with argon for 10 min before measuring. The current gradients were recorded with the potential scanned from -2 V to 2.5 V at 25°C.

Electrical impedance measurement

Impedance measurements were carried out by using a multichannel potentiostat (VSP300, BioLogic Ltd.). The frequency range was from 0.1 Hz to 100 kHz and the alternating signal was 10 mV. The results were recorded with a bias in relation to theV_{OC} of 600 mV in the dark. The obtained spectra were fitted using Z-View software corresponding to the appropriate equivalent circuit.

3. Results and discussions

Effect of NS on the chemical and photophysical properties of isolated composites based on Mo_6 cluster

It was suspected that the halogen groups of the $[\{Mo_6I^i_8\}I^a_6]^{2-}$ cluster unit hinder the charge transport in photovoltaic devices due to the difficulty in creating covalent bonding with functional groups on the lattice of the semiconducting surface. In order to improve the interactions between the cluster-based sensitizer and the charge collector surface, the replacement of the apical iodide ligands by aromatic sulfonate groups was investigated. In this study, the modification of the apical iodide ligands of the crystalline Mo_6 cluster precursor ($Cs_2[\{Mo_6I^i_8\}I^a_6]$) was carried out by using ($-OSO_2-C_{10}H_6-SO_3^-$)(NS) anions with two sulfonate groups. In general, the apical I ligand could be replaced by water molecules in a dispersing medium of acetone and distilled water to form a slightly modified cluster $[Mo_6I^i_8I^a_4(H_2O)^a_2]$ [19, 33]. The addition of functional ($-OSO_2-C_{10}H_6-SO_3^-$) groups to the medium should lead to a parallel substitution of the apical iodides to form the $[Mo_6I^i_8I^a_6(H_2O)^a_y(OSO_2-C_{10}H_6-SO_3^-)^a_{6-y}]^{y-2}$ ($0 \leq y \leq 6$) anionic cluster, which is neutralized by sodium cations. To confirm this exchangeability, the chemical element compositions of the modified Mo_6 cluster were investigated by X-ray spectroscopy (Fig. S1a). Table S2 summarizes the binding energies of the O1s, C1s, S2p, Na1s, Mo3d, and I3d regions that were calibrated using the carbon binding energy at 285 eV. The element compositions of the non-isolated and isolated MINS24 compounds are shown in Table S3. The complete elimination of the Cs^+ counter cation was confirmed after isolation. Moreover, the atomic ratio of the Mo and I atoms of the Mo_6 cluster in the isolated MINS24 compounds was obtained at 6 and 11 while the theoretical value of the Mo_6 precursor is 6 and 14. The elimination of three apical iodide ligands from the cluster precursor was suggested. The energy binding peaks specific to C1s, S2p, and Mo3d were respectively recorded at 285 eV, 168.3 eV, 228.9 ($Mo3d^{5/2}$), and 232.1 eV ($Mo3d^{3/2}$) (Figs. S1b-d). In greater detail, two peaks of Mo3d are specialized for the Mo^{4+} state of the Mo-I bonding of the Mo_6 cluster. According to the deconvolution spectrum of the O1s region in Fig.

1a and calculated data listed in Table S4, three contributions are observed. The binding energy peaks at 533.7 eV and 532.5 eV are assigned, respectively, to O=S and O-H coming from naphthalene sulfonate and H_2O apical ligands of the Mo_6 cluster. The peak centered at 530.9 eV is attributed to the formation of the O-Mo bonds due to the substitution of the O-containing apical ligands [34]. As seen in Fig. 1b, the deconvoluted energy peaks denoted for inner and apical iodide ligands (I^i and I^a) are indicated at 620.5 eV ($3d^{5/2}$) and 632.0 eV ($3d^{3/2}$) and 618.9 eV ($3d^{5/2}$) and 630.4 eV ($3d^{3/2}$), respectively. From Table S5, the calculated amount of the inner and apical iodides is 8 and 3 atoms, respectively, which agrees with 11 apical iodides in Table S3. Based on the deconvolution of the XPS spectra of O1s and I3d regions, a new cluster with the formula $[Mo_6I^i_8I^a_3(H_2O)^a_y(OSO_2\text{-}C_{10}H_6\text{-}SO_3^-)^a_{3-y}]^{y-2}$ ($0 \leq y \leq 3$), which is neutralized by sodium cations, is proposed. As seen in the element of compositions of MINS24 from Table S3, the sodium cations after isolation are realized at 3 atoms per one Mo_6 cluster unit. It is suggested that the MINS24 compound should include a cluster with the formula $[Mo_6I^i_8I^a_3(H_2O)^a_2(OSO_2\text{-}C_{10}H_6\text{-}SO_3^-\ Na^+)^a]$ and $Na_2(OSO_2\text{-}C_{10}H_6\text{-}SO_3^-)$ molecule at similar percentages.

Fig. 1c provides information about the Raman spectra of the MI and isolated MINS compounds with specific assignments for the Mo-I and Mo-Mo bonds in the wavenumber range from 50 to 400 cm^{-1}. According to the calculated data for the $[\{Mo_6I^i_8\}I^a_6]$ cluster reported by Schoonover et al., the proposed assignments are presented in Table S6. Considering the Raman shifts of MI, specific assignments recorded at 109 and 285 cm^{-1} belong to the symmetry vibration of the Mo-Mo bond of the octahedral Mo_6 cluster. The Raman shifts of Mo-I^a and Mo-I^i are recorded at 126 (Mo-I^i, Mo-I^a), 154.8 (Mo-I^i, A_{1g}), and 223 (Mo-I^i). In addition, the vibrational signals assigned to the Mo-O bonding appear at 487, 564, 726, and 955 cm^{-1} (**Fig. 1d**) [35]. Based on the NS reference sample, the Raman shift bands centered at 521 (C-C-C bending), 1054, and 1381 cm^{-1} (C-C stretching) are assigned to the C-C bond in naphthalene; 611 and 1119 cm^{-1} assigned to the S-O bond in the sulfonate ($-SO_3^-$) group; 1468 (C-H bending), 1566, and 1624 cm^{-1} assigned to the C-C and C=C stretching in an aromatic ring with resonances of the S-O vibrations [36-38]. In general, all the Raman bands of the MINS series show a similar signal. In comparison with the Raman bands of MI and NS, the MINS band is composed of vibration signals of its compositions with a slight modification. The recognition of specialized vibrational bands in the spectrum of MINS24 confirms the shift in the Raman peaks at a lower wavenumber for the Mo-I^i, Mo-I^a, Mo-O, S=O, and S-O stretching vibrations. For example, all the Raman peaks assigned to Mo-I^i and Mo-I^a, namely, at 125 (Mo-I^i, Mo-I^a), 151 (Mo-I^i, A_{1g}), and 219

cm^{-1}(Mo-I^i) are shifted towards lower wavenumber values. The contribution of the new Mo-O link thus affects the polarization and atomic distance of the Mo-I^i or Mo-I^a or Mo-Mo links. In addition, the intensity of the Raman peaks centered at 1561 and 1624 cm^{-1} is reversed in MINS24 compared to that of NS (**Fig. 1d**). Both Raman shifts are assigned to the symmetry C=C vibration in the ring that links carbon with the SO_3 stretching. Thus, the shift in the Raman peak from 1566 to 1561 cm^{-1} and the decrease of the signal intensity at 1623 cm^{-1} come from the increase of the defects in the S-O stretching due to the appearance of the possible Mo-O-S link [39]. The reduction of the polar vibrations of the S-O bond results in increasing the Raman scatterers. Fourier-transform infrared spectroscopy (FTIR) curves were obtained between 1300 cm^{-1} and 1000 cm^{-1} that characterize the vibrational band of the SO_3^- group during the interaction with anions (**Fig. 1e**). Most of the symmetric and asymmetric stretching vibrations assigned to SO of the SO_3^- group shift to a lower wavenumber. It is evident that a strong peak at 1046 cm^{-1} comes from the SO shifts to 1042 cm^{-1} and 1030 cm^{-1} after incorporating the Mo_6 cluster. Following the report of Kabiri and co-authors, the SO vibration appeared at around 1036 cm^{-1} and indicated the SO vibration in the free SO_3^- group [40]. The addition of sodium or calcium cations will provide ionic interactions that hindered the efficient delocalization of the negative charge on the sulfonate, resulting in the shift to 1044 and 1056 cm^{-1}, respectively. These proofs are meaningful to favor the appearance of the 1042 cm^{-1} and 1030 cm^{-1} peaks coming from SO after separating sodium cations in this study. The intensity of the 1030 cm^{-1} peak is strongly recognized in the case of MINS16 then it reduces for MINS24 and MINS35. The free SO_3^- groups in MINS16 are efficiently generated while the use of high NS amounts in MINS35 does not contribute to the separation of the sodium cations. In summary, as illustrated in Fig. 1f, at least one covalent bond possibly appears between the Mo_6 cluster and NS *via* the Mo-O-S bridge. Moreover, other SO_3^- groups could be paired with sodium cations or create ionic interactions between them that will depend on the added amounts of NS. The balance between the two kinds of ionic interactions possibly controls the aggregation of the nanoparticles that affect the homogeneous dispersion on the semiconductor substrate.

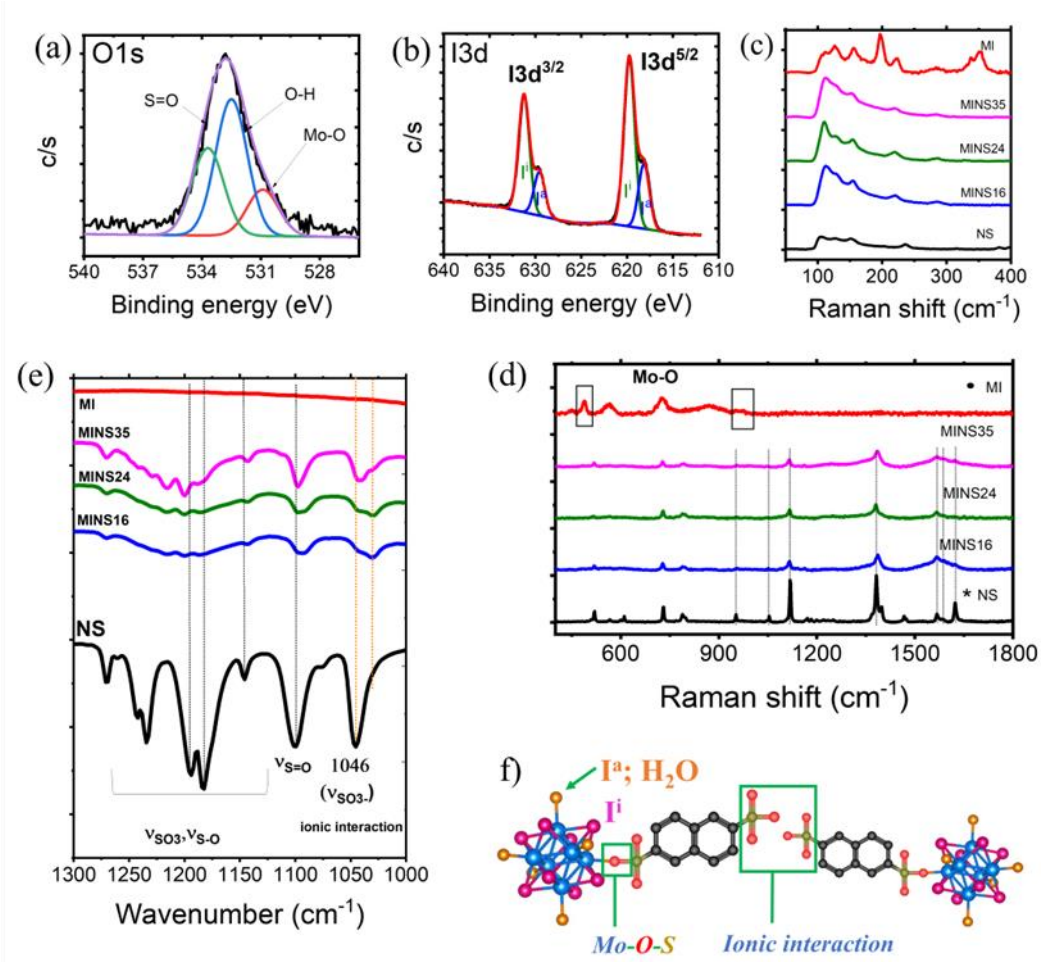

Figure 1. The deconvolution XPS spectra of a) O1s and b) I3d regions of the isolated MINS24. The fingerprint Raman shifts of MI, NS, and isolated MINSx (x=16, 24, 35) between c) 50 to 400 cm^{-1} and (d) 500 to 1800 cm^{-1} in air at 298K. e) Fourier-transform infrared spectroscopy (FTIR) curves between 1300 cm^{-1} and 1000 cm^{-1}. F) The schematic illustration of the chemical structure of the modified Mo_6 clusters and possible interactions.

The UV-Vis absorption spectra of the isolated $MINS_x$ (x=16, 24, 35) and electrophoretically deposited MI films on ITO-coated glass are summarized in **Fig. 2a**. As known, free NS molecules in the compound do not show absorption in the visible light range so they do not contribute to these absorption characteristics in Fig. 2a. The strong absorbance in the visible light range between 400 nm and 600 nm is realized for the electrophoretically deposited MI mainly containing $[Mo_6I^i_8I^a_4(H_2O)^a_2]$ clusters. The modification of the chemical compositions by replacing the iodide apical ligands results in a significant difference in the optical properties. In greater detail, the reduction of the visible light absorption is recognized for $MINS_x$ (x=16, 24, 35) films in the range between 500 nm and 600 nm.

Consequently, the optical gap energies also result in a clear change for all the $MINS_x$ (x = 16, 24, 35) cluster compounds as seen in **Fig. 2b**. As seen in Table 1, the optical energy gap increases from 2.08 eV for MI to around 2.44 eV for MINS16 and 2.6 eV for MINS24 and 35. The energy band gap of the $[Mo_6I^i_8I^a_4(H_2O)^a_2]\cdot mH_2O$ cluster recorded at 2.08 eV agrees with a previous study for the electrophoretically deposited Mo_6 thin film [19, 27]. In the case of MINS16, two energy gaps were calculated at 2.08 and 2.44 eV, which emphasize an incomplete apical exchange to form the constituting clusters; i.e., $[Mo_6I^i_8I^a_4(H_2O)^a_2]$ and $[Mo_6I^i_8I^a_3(H_2O)^a_2(\text{-}OSO_2\text{-}C_{10}H_6\text{-}SO_3^-\ Na^+)^a]$. The complete modification from the $[Mo_6I^i_8I^a_4(H_2O)^a_2]$ cluster to the $[Mo_6I^i_8I^a_3(H_2O)^a_2(\text{-}OSO_2\text{-}C_{10}H_6\text{-}SO_3^-\ Na^+)^a]$ cluster results in a proper change in the optical bandgap E_g that occurs for the MINS 24 and 35 compounds recorded at 2.6 eV.

To estimate the HOMO and LUMO energies of the new compounds and the electrochemical energy band gap, cyclic voltammetry measurements of the MI and isolated MINSx (x=16, 24, 35) compounds in acetonitrile with the calibration of the ferrocene/ferrocenium redox system are summarized in Fig. S2 and Table 1. The calculation is illustrated in Section 2.5. The onset of oxidation increases from 1.43 for the $[Mo_6I^i_8I^a_4(H_2O)^a_2]$ cluster to 1.76, 1.78, and 1.73 eV for the MINS16, MINS24 and MINS35 suspensions containing the $[Mo_6I^i_8I^a_3(H_2O)^a_2(\text{-}OSO_2\text{-}C_{10}H_6\text{-}SO_3^-\ Na^+)^a]$ clusters, respectively. It is evident that the aromatic sulfonate groups increase the stability of the cluster complex toward oxidation in the electrolyte medium. The obtained stability is an advantage for the application of the Mo_6 cluster in solar cells. In the negative potential region, the onset of reduction is similar to around -0.87 eV. The HOMO energies are significantly different between the two kinds of cluster complexes. These results show a similar trend to the reported data for the molybdenum cluster complexes $(nBu_4N)_2[\{Mo_6X_8\}X_6$ (X^- = Cl^-, Br^-, I^-) that have exchanged apical ligands by different aromatic sulfonate ligands [20]. The E_{HOMO} and E_{LUMO} of the modified Mo_6 complexes were systematically tuned by changing the electron-donating naphthalene and electron-withdrawing sulfonate in NS [41]. In greater detail, the electron-withdrawing sulfonate group will contribute to the reduction of E_{HOMO} from -5.8 eV to -6.1 eV [42, 43]. It causes a decrease in the electron-electron repulsion that modifies the strength of the Mo-Mo bonds and electronegativity of the Mo_6 octahedron. The electrochemical energy bandgaps calculated from cyclic voltammetry (CV) graphs in Table 1 are relatively similar to the optical energy bandgap that was calculated from the Tauc plot (**Fig. 2b**). In summary, the CV-derived HOMO and LUMO energy levels of the Mo_6-based sensitizers are presented in Fig. 2c. These LUMO energies of the MI and isolated MINSx (x= 16, 24, 35) compounds are much higher than the

conduction band (CB) of the semiconductor (-4.0 eV for anatase phase TiO_2), while the HOMO energies are lower than the oxidation potential of the I^-/I_3^-electrolyte (-4.8 eV). This results in the possibility of electron injection into the semiconductor in the photovoltaic device [44]. In line with previous studies, the modified sulfonate-based Mo_6 cluster could be a good candidate for a photostable photosensitizer that provides the excited electrons to generate a short-circuit current in the MCSSCs.

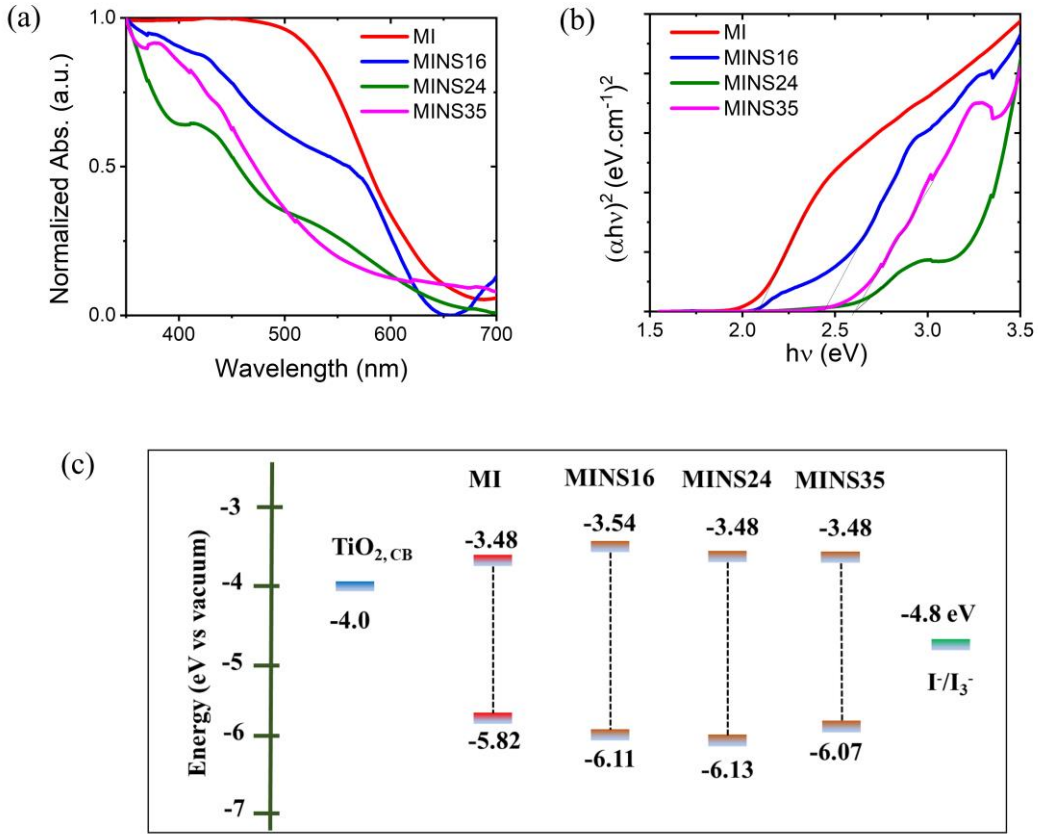

Figure 2. a) The absorption spectra of MI and isolated $MINS_x$ (x =16, 24, 35) on ITO-coated glass and b) the Tauc plots calculated from the absorption spectra for estimating the optical energy gap. c) CV-derived HOMO and LUMO energy levels vs vacuum of the Mo_6-based sensitizers.

Table 1. The potential of the onset of oxidation ($E^{onset, ox}$) and reduction ($E^{onset, red}$) and electrochemical energy band gap of the compound MI after EPD and isolated $MINS_x$ (x =16, 24, 35). The optical energy gap was calculated from the Tauc plot.

Composites	$E^{onset, ox}$ vs Ag/AgCl	HOMO level	$E^{onset, red}$ vs Ag/AgCl	LUMO level	Electrochemi-cal energy	Optical energy gap (eV)

	(V)		(V)		gap (eV)	
MI	1.47	-5.82	-0.87	-3.48	2.34	2.08
MINS16	1.76	-6.11	-0.81	-3.54	2.57	2.08; 2.44
MINS24	1.78	-6.13	-0.87	-3.48	2.65	2.59
MINS36	1.72	-6.07	-0.87	-3.48	2.59	2.60

Photophysical properties of the Mo_6 cluster-based photoelectrodes.

The isolated $MINS_x$ (x = 16, 24, 35) compounds were strongly aggregated after purification to eliminate the residual NS molecules and heat treatment at 50°C. The homogeneous dissolution was impossible to obtain in any solvent media. For that reason, the non-isolated MINSx slurries were directly used to deposit on the TiO_2 photoelectrodes to achieve a good uniform dispersion. As seen in the HR-TEM images of nanoparticles in the non-isolated $MINS_x$ slurries, the role of residual free NS molecules is discussed (Figs. 3a-c). The trends of the aggregated nanoparticles are different at various ratios of the NS and Mo_6 cluster precursors. The NS amount in MINS16 is efficient for reducing big Mo_6 crystals into nanoparticles sized from 70 to 100 nm while images of the MINS24 show a homogeneous dispersion of 5 nm-sized nanoparticles in the amorphous matrix containing the NS molecules. An increase in the NS amount of MINS35 causes an aggregation between these phases that disturbs the uniform dispersion of the modified Mo_6 cluster. It is evident that only the MINS24 slurries show a relative transparency (Fig. 3a-c). In general, in the solvent medium, big 1 µm-sized $Cs_2[\{Mo_6I^i_8\}I^a_6]$ crystals will be dissociated to form Cs^+ and $[\{Mo_6I^i_8\}I^a_6]^{2-}$ ions. These $[\{Mo_6I^i_8\}I^a_6]^{2-}$ ions tend to change a neutral $[Mo_6I^i_8I^a_4(H_2O)^a_2]$ cluster form that has strong hydrogen bonding causing an aggregation. In MINS24, most of the $[Mo_6I^i_8I^a_4(H_2O)^a_2]$ cluster is modified to the $[Mo_6I^i_8I^a_3(H_2O)^a_2(\text{-}OSO_2\text{-}C_{10}H_6\text{-}SO_3^-Na^+)^a]$ cluster surrounded by the negative charged NS that results in only an ionic interaction, preventing the aggregation. The elimination of residual NS surrounding MINS will destroy the monodispersed distribution that hinders the absorbed sensitizer amounts.

In this study, the titanium (IV) chloride surface treatment on TiO_2 was performed to improve the charge transport, thus enhancing the photovoltaic performance [31, 45]. The optical energy bandgap of TiO_2 was measured at 3.43 eV by using the Tauc plots in Figure SI3a which were almost similar to the previous report [46]. The mesoporous TiO_2 film with the essential anatase crystalline phase was

successfully prepared by thermal treatment at 550 ºC in air and its morphology was demonstrated in Figs. S3b and **3d**. The surface of the transparent TiO_2-based photoelectrodes is observed to have a roughness as well as high porosities that provide efficient active areas for anchoring the Mo_6 cluster. These patterns are stable and the porous morphology between the nanoparticles is connected after being treated with the $TiCl_4$ solution (Fig. **3e**). MI was deposited on the TiO_2 film by EPD for 2 minutes at 20 V. Compared to the soaking method, the EPD was reported as the best method to chemisorb the homogeneous MI into the TiO_2 mesoporous electrodes [19]. In the case of the non-isolated $MINS_x$ (x = 16, 24, 35) clusters dissolved in water/acetone, a vacuum impregnation process for 15 minutes was applied for the depositions because it was not successfully deposited by EPD. The distribution of MI into the cross-section area of the mesoporous TiO_2 film was demonstrated by using TEM-EDX mapping (Fig. S4). Besides the amount of MI adsorbed inside the TiO_2 pores, the thick layer of MI could be recognized on the top of the TiO_2 surface with a thickness of 0.7 µm. Similar layer structures were confirmed in the TiO_2-introduced MINS16 clusters by cross-section SEM images (Fig. S5). The MINS16-based photoelectrode possesses a thickness of 5.6 µm of which about 0.5 µm is only composed of MINS16 on the top. Fig. **3f** shows the smooth and homogeneous distribution of MINS24 on the surface of the TiO_2 film. These top cluster layers decrease in the MINS24-based film and disappear in the MINS35-based film (Fig. S6). The elemental compositions of the cross-section clarify the concentration of MINS16 as seen in Fig. SI5 and MINS24 in **Fig. 3g**. A highlight-colored layer assigned to the Mo, I, and S atoms properly appears on the top of the MINS16 while it does not focus on the top of the MINS24 film. Considering the similar deposition method for MINS16, 24, and 35 with a similar concentration of the $[Mo_6I_{14}]$ precursor, the difference in the deposition comes from the different number of NS molecules. The increase in the concentration of the NS functional groups seems to improve the adsorption of the cluster inside the pores and reduces the aggregation of clusters on the surface.

The elemental compositions and binding energy were measured for the MINS24 deposited on the TiO_2 film, showing the stability of the apical ligands after being introduced into the TiO_2 electrode (Tab. S3). The deconvolution spectra of the O1s regions and calculated data presented in Figs. 3**h** and Table S7 indicate the existence of binding energies assigned to the Mo-O and Ti-O links at about 530.7 eV, O-H at 532 eV, and O=S at 533.1 eV. The ratio between Mo and I at 6 and 11 means the link between MINS and the TiO_2 lattice should come from the sulfonate groups (SO_3^-) on NS (Tab. S8 and **Fig. 3i**). The binding energy spectrum of the Ti region shows two spin-orbit peaks of $2p^{3/2}$ (459.4 eV) and $2p^{1/2}$

(465.2 eV) (**Fig. 3k**). It is difficult to show the difference in the binding energy of the Ti-O bonding in TiO_2 or Ti-O-cluster links. The possible prediction for the linking between the SO_3 group-functionalized cluster and TiO_2 lattice could occur; the SO_3 group reacted with the OH groups on the lattice and eliminated water produced during heating at 120 ºC to form a Ti-O-S(O_2)-cluster bridge. This covalent interaction should favor the charge transport inside the photoelectrode and should lead to a higher efficiency of photovoltaic devices.

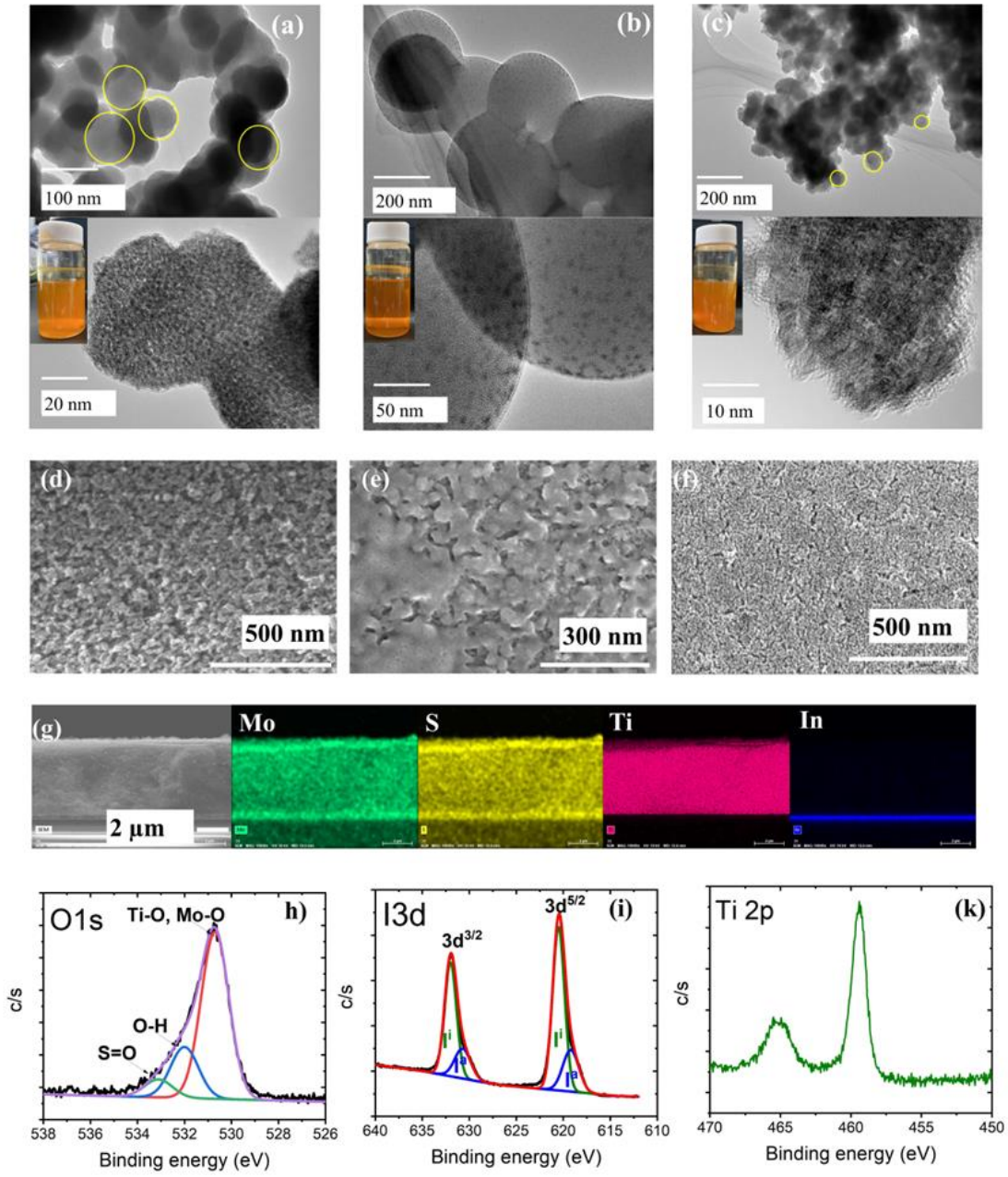

Figure 3. HR-TEM images at different magnifications and photographs of non-isolated slurries under visible light irradiation of a) MINS16, b) MINS24, and c) MINS35. Scanning electron microscopy (SEM) images of d) mesoporous TiO_2-based film, e) mesoporous TiO_2-based film treated with $TiCl_4$ 0.3M, f) the non-isolated MINS24-coated TiO_2 photoelectrode. g) the SEM-EDX mapping of the cross-section of non-isolated MINS24-coated TiO_2 photoelectrode. The multiplet split components of h) XPS O1s spectrum, i) XPS I3d spectrum, and (k) XPS Ti2p spectrum.

The evaluation of the photosensitizer efficiency in solar cells relates to the emission maximum wavelength (λ_{em}), photoluminescence lifetime (τ_{em}) as well as the excited state lifetime and quantum yield (Φ_{em}). To identify the photoluminescent property (PL) of the Mo_6 cluster in solar cells, crystalline MI or isolated MINS-coated quartzs were irradiated under 365 nm UV light (Fig. 4a). The PL intensity of MI is weak while well-distinguished peaks centered at 638, 642, and 646 nm appear for the isolated $MINS_x$ (x= 16, 24, 35), respectively. These broadly obtained PL emissions belong to the wavelength range from 580 nm and 700 nm that is excited by light irradiation lower than 500 nm (Fig. 4b). This large Stoke shift will limit the loss of the absorption photonic energy. These results agree with the previous report on the exchange of different aromatic sulfonate ligands [20]. In summary, the enhancement of the PL signal in MINS means an increase in the contribution of the radiative recombination process compared to the non-radiative recombination [47]. Non-radiative recombination is an unwanted process in the photovoltaic characteristics due to lowering the light generation efficiency by phonon scattering and increasing heat losses.

Time-resolved photoluminescence (TRPL) signals were recorded via Time-Correlated Single Photon Counting (TCSPC) in air at 298 K. The luminescence emissions of the MI and MINSx (x= 16, 24, 35) composites are indicated at the wavelength of 700 nm and 640 nm irradiated under 361 nm UV light, respectively. The decay time profiles of MI and MINS crystalline on quartz or TiO_2 are presented in Fig. S7-8. The luminescence lifetimes were fitted by 2 exponential decays for MI-based samples and 3-exponential decays for the MINSx-based samples summarized in Table S9 and (**Fig. 4c**). The fitted data of MI deposited on quartz show an average emission lifetime (τ_e) of 1.172 μs that includes a high real percentage of about 98.1 % (τ_1 = 58 ns) and the other is 1.9 % (τ_2 = 58.7 μs). This is in agreement with the emission lifetime of the Mo_6-based clusters reported in the μs range [20, 26]. The shorter lifetime is caused by the aggregated clusters while another comes from the monodispersed clusters.

The emission lifetimes of the isolated $MINS_x$ (x = 16, 24, 35) deposited on quartz were fitted by a 3-exponential decay calculation. The contribution of the emission lifetime (τ_3) in the μs range is almost zero while a new and short emission lifetime (τ_2) in the ns range appears as seen in Table S9. Apparently, the photoexcited electron density could be rearranged and trapped by the π-spacer group as naphthalene of MINS, thus tuning the photo-driven electron transport and shortening the lifetime (τ_2) [48-49]. Consequently, the average lifetimes were calculated at 27, 47, and 60 ns for the isolated MINS16, MINS24 and MINS35, respectively. This trend is reversed in the non-isolated $MINS_x$ samples deposited on quartz and relatively similar emission lifetimes were calculated at 48, 47, and 41 ns. Generally, the NS molecules contribute to the reduction of the emission lifetime by the electron-withdrawing sulfonate groups. The sulfonate acceptors on NS in MINS possibly accelerate the recombination rate of the excited electrons causing a slight decrease in the emission lifetime with different amounts of NS. The sulfonate functional group has already been investigated as an acceptor to balance the charge carrier transport, enhance the moisture resistance, and reduce the migration of photosensitizers for enhancing the performances of perovskite solar cells [50, 51].

In order to deeply understand how the charge recombination on the Mo_6 cluster occurs on the interface of the photoelectrode, the luminescence lifetimes of the MI and non-isolated MINS clusters homogeneously deposited on the mesoporous TiO_2 photoelectrode were investigated (Fig. 4c). As demonstrated in Tab. 1, the LUMO energies of MI and MINS are -3.48 eV which are compatible with the injection into the conduction band (CB) at -4.0 eV of TiO_2. All the emission lifetimes of MI and non-isolated MINS compounds deposited on the TiO_2 substrate result in a reduction the same as the increase in the recombination rate by 2 times. MI obviously shows an efficient electron injection into the CB of TiO_2 when the emission decreases from 1170 ns to 72 ns. This electron injection rate increases by 3 times after introducing NS molecules (~ 21 ns). MINS35 obtains a saturated recombination rate (~ 20 ns). As discussed before, the compositions of the sensitizer adsorbed in TiO_2 will be composed of $[Mo_6I^i_8I^a_3(H_2O)^a_2(OSO_2\text{-}C_{10}H_6\text{-}SO_3^-\ Na^+)^a]$ and free $Na_2(OSO_2\text{-}C_{10}H_6\text{-}SO_3^-)$ molecules for MINS24 and the free NS molecules will increase more in MINS35. Here, NS plays some essential roles for improving the electron injection: i) the free NS improves the adsorption and homogeneous distribution of MINS on the surface of the lattice, and ii) NS incorporated with the MI cluster efficiently orientates the photoexcited electron on the Mo_6 cluster to the conduction band of TiO_2 via the Mo-O-(OSO_2-$C_{10}H_6$-SO_2)-O-Ti link [52]. The concentration of free NS molecules in MINS24 conducts a fast injection of the photoinduced electron into the TiO_2 photoelectrode that

continues to accelerate the injection of the higher free NS concentration in MINS35. It is predicted that the electron-withdrawing sulfonate contributes to the recombination of the photoinduced electrons. Interestingly, many studies have reported efforts to prolong the emission lifetime of sensitizers to higher than 0.1 ns while the Mo_6 cluster is feasible to adjust the emission decay time in the range from ns to µs by changing the apical ligand [16].

As expected, an increase of the quantum yield (Φ_{em}) with the functionalization of the cluster with NS and almost similar values at different NS ratios are due to an increase in the radiative recombination or photoluminescence signal (**Fig. 4d**). In general, free NS molecules only show an optical absorption in the UV range with a peak centered at 314 nm in a water solution and thus shows no contribution to the absorbance of MINS in the visible range higher than 400 nm (Fig. S9a). NS also does not affect the optical characteristic of the TiO_2 photoelectrode as seen in Fig. S9b. These low quantum yield values are recorded at about 1.2 % due to the high scattering from solid crystals.

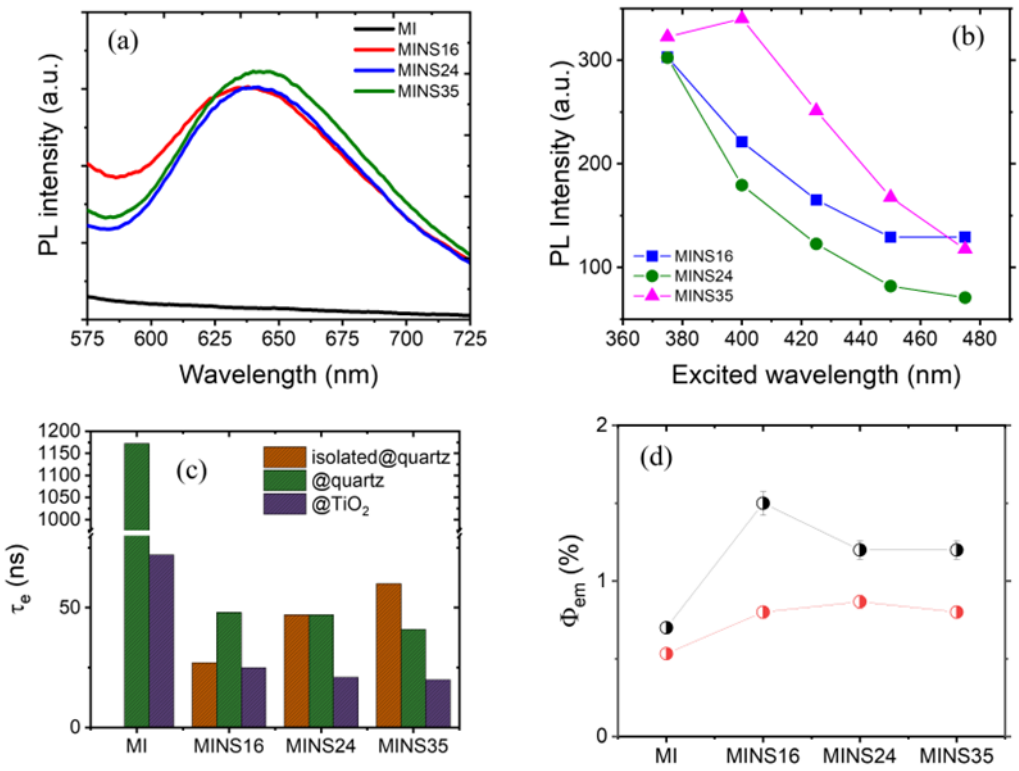

Figure 4. a) Emission spectra of the MI and isolated MINSx (x=16, 24, 35) compounds deposited on quartz under irradaiation at 365 nm UV light. b) The luminescent emission intensity of the isolated $MINS_x$ upon light illumination at different wavelengths. c) Average emission lifetime and d) quantum

yield of MI and non-isolated or isolated MINSx deposited on quartz (black circles) and TiO_2 substrate (red circles) under excitation at 361 nm.

Photovoltaic characteristics of the Mo_6 cluster-based photoelectrodes.

The J-V characteristic of MCSSCs was measured for a photoanode containing the TiO_2 layer adsorbed MI and MINSx (x=16, 24, 35) clusters at about 5-µm thickness (Fig. 5). A series of isolated $MINS_x$ (x= 16, 24, 35)-based MCSSCs were performed for reference. The short-circuit current (J_{sc}), open-circuit voltage (V_{oc}), fill factor (FF), and power conversion efficiency (η) are listed in Table SI10 and **Fig. 5a**. The MI and isolated MINS-based MCSSCs show different J_{sc} and V_{oc} values. In a previous report, an electrophoretically MI-based MCSSC was reported with V_{oc} values of 529 mV, J_{sc} of 1.13 mA/cm^2, FF of 74 and η of 0.44% [19]. In this study, an electrophoretically MI-based MCSSC, with similar I^-/I_3^- electrolyte compositions, was remade under similar conditions. The photovoltaic parameters were measured at 600 mV, 1.76 mV, 50 and 0.52 % for the MI-based MCSSC. As demonstrated in Table S10, all the isolated MINS-based MCSSCs present a reduction in J_{sc}, however, FF definitely increases from 0.5 for MI to 0.65. It is evident of an enhancement of the charge transfer through NS which is linked with the Mo_6 cluster. Only the MINS24-based cell shows a higher overall efficiency (0.58%) compared to the MI-based cell. This result proves the role of NS in enhancing the photoexcited electron injection process from the cluster to CB of the semiconductor. It agrees with a discussion of the emission lifetime parts. Although the slight change of the PV parameters in cells occurred during continuous measurement under irradiation for 330s, the overall efficiency was retained. Fig. S10 presents the morphologies and nanoparticle dispersion of the isolated MINS16 and MINS24. It is a fact that the 1 µm-sized big nanoparticles and most of the small nanoparticles were deposited on the surface of the TiO_2 substrate. This is a result of a weak dissolution in the solvent medium seen in Fig. S10. The interface connection between the absorbed Mo_6 cluster and the active site of TiO_2 is not efficient.

Fig. 5b and Table 2 demonstrate the photovoltaic characteristics of the non-isolated $MINS_x$-based MCCSCs. MI and MINS16 give a slightly different short circuit current J_{sc} of about 1.76 and 1.95 $mA.cm^{-2}$, respectively, but the fill factor is enhanced from 0.5 to 0.59 for the MINS16-based MCSSC. The improvement of the fill factor with the appearance of the NS ratios tends towards the first hypothesis. Moreover, this phenomenon occurs without an increase in the recombination rate since the V_{OC} is stable. This result provides proof for the discussion in Fig. 4c with the positive effect of the NS

on electron transport and electron injection efficiencies. As a result, the PCE of MINS16-based MCSSC increases by 31% compared to the previous study [25]. the MINS35-based MCSSC shows the highest short circuit current J_{sc} of 2.56 mA.cm^{-2} corresponding to the highest PEC of 0.97 % while the fill factor of MINS24-based MCSSC is more efficient. Considering the short-circuit current J_{sc}, MINS35 obtains a good ratio between MI and NS for a high PEC at 0.97 %, increasing 90 % in comparison to the MI-based MCSSC. The incident photo-to-current efficiency (IPCE) plots of MI and non-isolated MINSx (x=16, 24, 35)-based cells provide proof that supports the high PCE of the MINS24 and MINS35-based cells (Fig. 5c). For a comparison of the PV performance of the non-isolated and isolated $MINS_x$- based MCSSCs, the NS linked with the Mo_6 cluster will enhance FF the same as the electron injection while the free surrounding NS will enhance the Mo_6 absorption and photocurrent.

The efficient IPCE in the visible light range is obtained for MINS24 and 35 recorded at 23 % with a wavelength centered at 430 nm and 7% with a wavelength centered at 500 nm. Using an electron-donating organic monolayer at an organic/inorganic interface has proven the induction of the band bending that depends on the adsorbing molecule concentration [53]. The effect of band bending will accelerate the electron transfer at the interface of the NS-modified Mo_6 cluster to the TiO_2 semiconductor until equilibrium is reached [54, 55]. In this study, the concentration of the free NS molecules is controlled to obtain the optimal effect of band bending for charge transfer efficiency.

Interestingly, the MI and non-isolated $MINS_x$ (x = 16, 24, 35) -based cells first showed the rising trend of PCE under irradiation of simulated solar light (Fig. 5d). All the cells present a rising tendency of the PCE of about 20 % after various cycles and then retain or gradually reduce. This phenomenon does not occur for the isolated-$MINS_x$-based MCCSCs. The rising PCE mostly comes from the enhancement of the photocurrent as seen in Tab. 2. The MI-based cell reaches a maximum PCE after 80s then gradually decreases until 330 seconds with a PCE (0.44 %) that is lower than that of the first cycle (0.52 %). Here, two points need to be considered; the long emission lifetime (72 ns) of MI can accumulate the photocurrent in the first 80 seconds, then the recombination rate occurs faster than the accumulation rate due to a generation of a new radical composition which catches the excited electron. It is suggested that the water adsorbed in the $[\{Mo_6I^i_8\}I^a_4(H_2O)^a_2].xH_2O$ cluster of the MI-based cell could be hydrolyzed to form hydroxyl radicals that collect the electrons, suppressing the electrolyte and cluster regeneration. However, this phenomenon does not occur in both the MINS16 and MINS24-based cells that show similar trends of PCE with a peak of the PCE at values of 0.82 % and 1.18% and

then retain it up to 330 seconds. The increase in the PCE at the first stage relates to the long emission lifetime of the $\{Mo_6I^i_8\}^{4+}$ core (~ 20 ns), demonstrating a slow recombination of photoexcited electrons on clusters and accumulating in the total current. In the second saturation state, the free naphthalene group on NS around the Mo_6 cluster can trap the electron by electron-electron pulsion and slow down the recombination process on the Mo_6 cluster. At the suitable ratios of the Mo_6 cluster precursor and NS in MINS16 and MINS24, electron-electron pulsion efficiently works and the PCE is retained at 330 seconds of measurement (Fig. 5d). However, the PCE of the MINS35-based cell has a similar trend with MI; reaching a PCE peak at 1.13% then gradually reducing. At higher NS concentrations, the aggregation of NS could occur and the electron-withdrawing sulfonate and electron-donating naphthalene of the free NS can create a competition in charge recombination and charge trapping of the photoinduced electrons. When the electron-withdrawing sulfonate strongly contributes to the charge recombination, regeneration of the cluster will be suppressed resulting in a reduction of the accumulation of the photocurrent as seen in the PCE tendency of the MINS35-based cell. The morphology of the MINS24-based electrode after photovoltaic measurement for 330 seconds and washing the electrolyte by using acetone is presented in Fig. 5e. It can be clarified that the original surface is retained with the confirmation of Mo atoms from the Mo_6 cluster on the surface (Fig. 5f).

The photovoltaic characteristics can provide interesting information: i) control of the concentration of NS to obtain a suitable emission lifetime for the $\{Mo_6I^i_8\}^{4+}$ core that accumulates the photocurrent, i) NS can enhance the photocurrent J_{sc} and fill factor that comes from the improvement of the electron transport by inducing band bending, and iii) clarify the relation between the MS concentration on the PEC of the MCSSC.

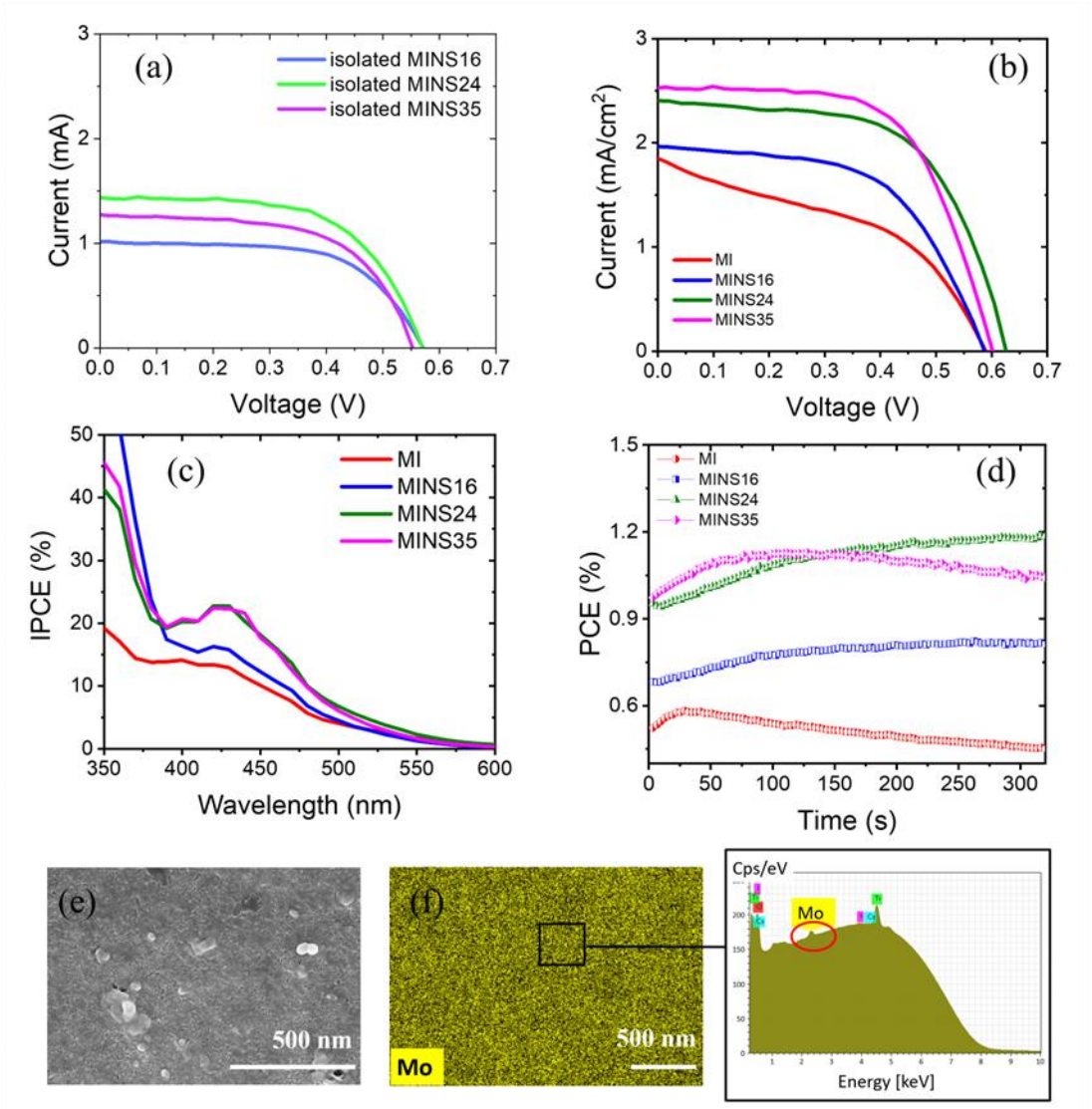

Figure 5. a) J-V characteristic curves of isolated Mo_6 cluster-based-MCCSCs. b) J-V characteristic curves, (c) IPCE curves, and (d) PCE tendency for 100 cycles (330 s) of measurement of non-isolated Mo_6 cluster-based-MCCSCs. E) FE-SEM images and f) SEM-EDX mapping and element spectrum of the non-isolated MINS24-based photoelectrode after irradiation for 330s and elimination of the electrolyte.

Table 2. J-V characteristic of MI and non-isolated MINSx (x=16,24,35) cluster-based MCSSCs at first cycle. Values in brackets were recorded at maximum PCE.

Cell	J_{sc} ($mA.cm^{-2}$)	V_{oc} (mV)	FF	η (%)

MI	1.76 (1.96)	600 (600)	0.50 (0.50)	0.52 (0.58)
MINP16	1.95 (2.55)	600 (590)	0.59 (0.54)	0.68 (0.82)
MINP24	2.38 (3.14)	630 (630)	0.63 (0.6)	0.95 (1.18)
MINP35	2.56 (3.22)	610 (600)	0.62 (0.58)	0.97 (1.13)

Electrochemical behaviors of the MI and non-isolated $MINS_x$ (x=16, 24, 35)-based MCSSCs were investigated by measuring the charge transfer resistance R_{ct}, the sheet resistance R_s, and the pseudo capacitance CPE. Fig. 6a shows Nyquist plots of all cells fitted by using the illustrated equivalent circuit. The circuit is composed of two semicircles; the first semicircle corresponds to the substrate resistance (Rct_1) for which the onset represents the sheet resistance (R_s) of the photoelectrode and the second semicircle results in the impedance of the cluster/TiO_2/electrolyte interface (Rct_2) [31, 56, 57]. Bode plots of the cells provide the maximum angular frequency (ω_{max}) that is used to calculate the electron lifetime in the cells (Fig. 6b). Nyquist and Bode plots were measured in the frequency range from 100 kHz to 0.1 Hz at the open-circuit voltage (V_{oc}) of 600 mV under dark conditions. The charge recombination (τ_{rec}) ability at the cluster/TiO_2/electrolyte interface competes with the charge transport (τ_{trans}). The electron lifetime (τ_{rec}) is associated with ω_{max} in an equation; $\tau_{rec} = 1/(2\pi f)$. The calculated data are summarized in Tab. 3. It was clarified that MI with the longest recombination time (49.8 ms) is beneficial to suppressing the charge recombination on the cluster/TiO_2/electrolyte interface. The increase in the NS concentration causes a reduction in the charge recombination time (< 1 ms), however, it causes a decrease in Rct_2 corresponding to an improvement in the injection efficiency. The higher chemical capacitance ($C\mu$) of the MI-based cells results in the efficient suppression of the trapping/de-trapping process of the injected electrons in the conduction band of TiO_2 [58]. Although NS negatively affects the suppression of the trapping/de-trapping process, the MINS 24-based MCSSC shows the fastest electron transport (τ_{trans}) of 4.2 μs that is faster by 15 times in comparison to MI (τ_{trans} = 64.6 μs). This transfer rate starts to be saturated for the MINS35-based cells (τ_{trans} = 5.7 μs). It is consistent with the performances of the MINS24 and 35-based cells. The competition of the electron lifetime in electrolyte and electron transfer by using NS produces a good improvement in the PCE. For that reason, the control of the NS concentration is necessary in the investigations to improve the PCE. In summary, the charge collection efficiency (η_{cc}) derived from $\eta_{cc} = (1+ \tau_{trans} / \tau_{rec})^{-1}$ is about 99 % of all cells which is a beneficial characteristic for obtaining a high efficiency for photovoltaic devices [59, 60].

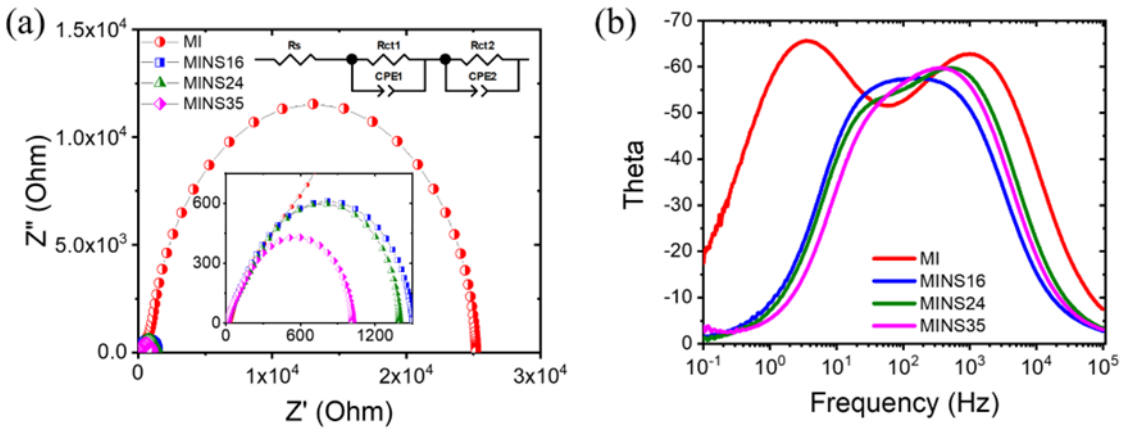

Figure 6. (a) Nyquist plots and equivalent circuits used for fitting the cell impedance and (b) Bode plots of the MI and non-isolated $MINS_x$-based MCSSCs (x=16, 24, 35).

Table 3. Comparison of EIS parameters of the MI and non-isolated $MINS_x$-based cells (x=16, 24, 35); sheet resistance R_s, charge transfer resistance $R_{ct,}$ and electrochemical capacitance CPE.

Cells based	R_s (Ω)	R_{ct2} (Ω)	ω_{max} (Hz)	τ_{rec} (ms) $\tau_{rec} = 1/(2\pi f)$	C_μ (μF) $C_\mu = \tau_{rec/Rct2}$	τ_{trans} (μs) $\tau_{trans} = C_\mu R_s$	η_{cc} (%)
MI	31.4	24142	3.2	49.8	2.06	64.6	99.9
MINS16	13.7	1188	144.5	1.1	0.93	12.7	98.9
MINS24	11.6	1157	380.1	0.42	0.36	4.2	99.0
MINS35	11.8	859	380.1	0.42	0.49	5.7	98.6

Although it is a challenge to improve the photovoltaic performance of metal atom cluster-based solar cells, this study has proved the possibility and understood the impact of the physicochemical properties of the cluster for improving the efficiency. In connection with the study, apical ligand groups on the cluster play an important role in enhancing the charge transfer which strongly contributes to the photovoltaic efficiency. For further strategies, some suggestions are proposed to obtain a higher efficiency, for example, the ligands should contain the electron donating groups functionalization; the co-sensitized dye will be investigated with the cluster; the maximal exchange to 6 apical ligands while retaining the visible absorption will be considered; different electrolytes will be used for improving the interaction with the cluster, etc.

4. Conclusion

The Mo_6-based MCSSCs were investigated for their photophysical, photoelectrochemical, and photovoltaic behaviors with the addition of aromatic sulfonate functional groups for the first time. The Mo_6 cluster was functionalized naphthalene-2,6-disulfonate (NS) groups by employing the chemical solution method at different molar ratios of the precursors. The study confirmed that the as-synthesized compounds were composed of the Mo_6-based clusters with the formula of $[Mo_6{}^{i}I_8{}^{a}I_3(H_2O)^{a}{}_2(\text{-}OSO_2\text{-}C_{10}H_6\text{-}SO_3^{-}\ Na^{+})^{a}]$ and free $Na_2(\text{-}OSO_2\text{-}C_{10}H_6\text{-}SO_3^{-})$ molecules. The broad absorbance in the visible range was lower than 500 nm, the photoluminescent emission had wavelengths centered around 640 nm, and the photoluminescence lifetime in the ns range on the TiO_2 substrate were verified as a function versus the concentration of the introduced NS. NS played a vital role in stabilizing the cluster in the redox mediator, increasing the distribution of the Mo_6-based photosensitizers in TiO_2, and improving the charge transfer process in the redox mediator. As a result, the MINS-based MCSSC resulted in a PCE of 0.97 % which was enhanced by 90 % in comparison to the MI-based cell. Interestingly, this PCE reached the highest value of 1.18 % and then became saturated at the highest value after 330 seconds of measurement for the best cell. A deep understanding of photophysical and photoelectrical behaviors is the original step in targeting the improvement of the efficiency of optoelectronic devices. The first basic knowledge of this study will open a new pathway for research on the improvement of the power conversion efficiency of MCSSCs based on octahedral transition metal clusters.

ASSOCIATED CONTENT

Supporting Information. XPS binding energy and deconvolution spectra; The cyclic voltammetry diagrams; XRD pattern of the TiO_2 film; cross-section SEM and SEM-EDX mapping images of the photoelectrode; Decay time profiles of the transient absorbance.

AUTHOR INFORMATION

Corresponding Author

Thi Kim Ngan NGUYEN, International Center for Young Scientists, National Institute for Materials Science (NIMS), 1-2-1 Sengen, Tsukuba, Ibaraki 305-0047, Japan

E-Mail address: NGUYEN.Thikimngan@nims.go.jp

Author Contributions

Thi Kim Ngan Nguyen conceived and designed the experiments; performed the experiments, analyzed and interpreted the data, and drafted the article. Fabien Grasset, Stephane Cordier and Adèle Renaud analyzed and interpreted the data; and drafted the article. Noée Dumait performed the CMI synthesis. Satoshi Ishii, Hiroshi Fudouzi, and Tetsuo Uchikoshi critically revised to improve the intellectual content.

Acknowledgments

These studies were carried out under the continued financial support of the International Center for Young Scientists (ICYS-Sengen), NIMS, and the France-Japan International Collaboration Framework (IRL3629 LINK, ANR-22-CE09-0015). T.K.N Nguyen would like to thank Dr. Suzuki Tohru for the laboratory supply, Dr. Naoto Shirahata for his useful advice on photoluminescence decay measurements and Dr. Irem Nur Gamze Ozbilgin for the PL decay and Raman's measurements. This study was supported by "Advanced Research Infrastructure for Materials and Nanotechnology in Japan (ARIM)" of the Ministry of Education, Culture, Sports, Science and Technology (MEXT); Proposal Number 23NM5289.

Notes

The authors declare no competing financial interest.

References

1. Munoz-Garcia; A. B., Benesperi; I., Boschloo; G., Concepcion; J. J., Delcamp; J. H., Gibson; E.A., Meyer; G.J., Pavone; M., Pettersson; H., Hagfeldt; A., Freitag; M. Dye-sensitized solar cells strike back. Chem. Soc. Rev., 2021, 50, 12450-12550.

2. Sharma; K., Sharma; V., Sharma; S. S., Dye-Sensitized Solar Cells: Fundamentals and Current Status. Nanoscale Research Letters, 2019, 13, 381-427.

3. Bade; B.R., Kore; K. B., Rondiya; S. R., Nilegave; D. S., Nasane; M.P., Jathar; S. B., Barma; S. V., Jadkar; S. R., Funde; A. M., Room Temperature Synthesis of Formamidinium Lead Iodide (FAPbI3) Perovskite for Low-Cost Absorber in Solar Cells. ES Energy & Environment, 2021, 13, 31-36.

4. Ma; Y., Zhang; Y, Liu; M., Han; T., Wang; T., Wang; X., Improving the performance of quantum dot sensitized solar cells by employing Zn doped CuInS2 quantum dots. Adv. Composites and Hybrid Mater., 2022, 5, 402–409 (2022).

5. O'Regan; B., Grätzel; M. A low-cost, high-efficiency solar cell based on dye-sensitized colloidal

titanium dioxide films. Nature, 1991, 353, 737–740.

6. Sen; A., Putra; M.H., Biswas; A.K., Behera; A. K., Groβ; A., Insight on the choice of sensitizers/dyes for dye sensitized solar cells: A review. Dyes and Pigments, 2023, 213, 111087.

7. Lin; L., Li; X., Zhang; H.,Xu B.B., Wasnik; P., Li; H., VirSingh; M., Ma; Y., Li; T., Guo; Z., Research progress of MXenes and layered double hydroxides for supercapacitors Inorg. Chem. Front., 2023,10, 4358-4392.

8. Hou; X., Aitola; K., Lund; P. D. TiO_2 nanotubes for dye-sensitized solar cells—A review. Energy Science & Engineering, 2020, 9, 921-937.

9. Ren; Y., Zhang; D., Suo; J., Cao; Y., Eickemeyer; F. T., Vlachopoulos; N., Zakeeruddin; S. M., Hagfeldt; A., Grätzel; M., Hydroxamic acid pre-adsorption raises the efficiency of cosensitized solar cells. Nature, 2023, 613, 60-65.

10. Song; H., Lin; Y., Zhang; Z., Rao; H., Wang; W., Fang; Y., Pan; Z., Zhong; Z., Improving the Efficiency of Quantum Dot Sensitized Solar Cells beyond 15% via Secondary Deposition. J. Am. Chem. Soc., 2021, 12, 4790–4800.

11. Chen; J. S., Choi; H., Kamat; P.V., Metal-Cluster-Sensitized Solar Cells. A New Class of Thiolated Gold Sensitizers Delivering Efficiency Greater Than 2%. J. Am. Chem. Soc., 2013, 135, 8822–8825.

12. Abbas; M. A., Kim; T.S., Lee; S.U., Kang; Y. S., Bang; J. H., Exploring Interfacial Events in Gold-Nanocluster-Sensitized Solar Cells: Insights into the Effects of the Cluster Size and Electrolyte on Solar Cell Performance. J. Am. Chem. Soc., 2016, 138, 390–401.

13. Sakai; N., Ikeda; T., Teranishi; T., Tatsuma; T., Sensitization of TiO_2 with Pt, Pd, and Au Clusters Protected by Mercapto- and Dimercaptosuccinic Acid. Chem. Phys. Chem., 2011, 12, 2415-2418.

14. Jennings; J. R., Liu; Y., Wang; Q., Efficiency Limitations in Dye-Sensitized Solar Cells Caused by Inefficient Sensitizer Regeneration. 2011, J. Phys. Chem. C, 115, 15109–15120.

15. Zhou; P., Liang; J., Lin; B., An; Z., Chen; R., Chen, X.; An; Q., Chen; P., Effect of the Spatial Configuration of Donors on the Photovoltaic Performance of Double D−π–A Organic Dyes. ACS Appl. Mater. Interfaces, 2021, 13, 40648–40655.

16. Zohry; A. E., Orthaber; A., Zietz; B., Isomerization and Aggregation of the Solar Cell Dye D149. J. Phys. Chem. C, 2012, 116, 26144–26153.

17. Warnan; J., Pellegrin; Y., Blarta; E., Odobel; F. Supramolecular light-harvesting antennas to enhance absorption cross-section in dye-sensitized solar cells. Chemical Communication, 2012, 48, 675-677.

18. Renaud; A., Grasset; F., Dierre; B., Uchikoshi; T., Ohashi; N., Takei; T., Planchat; A., Cario; L.,

Jobic; J., Odobel; F., Cordier; S., Inorganic Molybdenum Clusters as Light-Harvester in All Inorganic Solar Cells: A Proof of Concept. Chemistry Select, 2016, 1, 2284-2289.

19. Renaud; A., Nguyen; T.K.N., Grasset; F., Raissi; M., Guillon;V., Delabrouille, F., Dumait; N., Jouan; P.Y., Cario; L., Jobic; S., Pellegrin; Y., Odobel; F., Cordier; S., Uchikoshi; T. Preparation by electrophoretic deposition of molybdenum iodide cluster-based functional nanostructured photoelectrodes for solar cells. Electrochimica Acta, 2019, 317, 737-745.

20. Efremova; O.A., Vorotnikov; Y.A., Brylev; K.A., Vorotnikova; N.A., Novozhilov; I.N., Kuratieva; N.V., Edeleva; M.V., Benoit; D.M., Kitamura; N., Mironov; Y.V., Shestopalov; M.A., Sutherland; A.J. Octahedral molybdenum cluster complexes with aromatic sulfonate ligands. Dalton Trans, 2016, 45, 5427–15435.

21. Cordier; S., Grasset; F., Molard; Y., Amela-Cortes; Boukherroub; M. R., Ravaine; S., Mortier; M., Ohashi; N., Saito; N., Haneda; H., Inorganic Molybdenum Octahedral Nanosized Cluster Units, Versatile Functional Building Block for Nanoarchitectonics. Inorg. Organomet. Polym. Mater., 2015, 25, 189−204.

22. Nguyen; T.K.N., Lebastard; C., Wilmet; M., Dumaitc; N., Renaud; R., Cordier; S., Ohashi; N., Uchikoshi; T., Grasset; F., A review on functional nanoarchitectonics nanocomposites based on octahedral metal atom clusters (Nb6, Mo6, Ta6, W6, Re6): inorganic 0D and 2D powders and films. STAM, 2022, 23, 547–578.

23. Lappi; T., Cordier; S., Gayfulin; Y., Girard; S.A., Grasset; F., Uchikoshi; T., Naumov; N.G., Renaud; A., Nanoarchitectonics of Metal Atom Cluster-Based Building Blocks Applied to the Engineering of Photoelectrodes for Solar Cells. Solar RRL, 2023, 7, 2201037.

24. Nguyen; T. K. N., Dumait; N., Grasset; F., Cordier; S., Berthebaud; D., Matsui; Y., Ohashi; N., Uchikoshi; T., Zn−Al Layered Double Hydroxide Film Functionalized by a Luminescent Octahedral Molybdenum Cluster: Ultraviolet−Visible Photoconductivity Response. ACS Applied Materials & Interfaces, 2020, 12, 40495-40509.

25. Guégan; G., Cheng; X., Huang; X., Němečková; Z., Kubáňová; M., Zelenka; J., Ruml; T., Grasset; F., Sugahara; Y., Lang; K., and Kirakci; K., Graphene Oxide Sheets Decorated with Octahedral Molybdenum Cluster Complexes for Enhanced Photoinactivation of Staphylococcusaureus. Inorg. Chem. 2023, 62, 14243–14251.

26. Nguyen, T. K. N.; Grasset, F.; Cordier, S.; Dumait, N.; Ishii, S.; Fudouzi, H.; Uchikoshi, T. Light harvesting hexamolybdenum cluster integrated with the 3D ordered semiconductor inverse opals for optoelectronic property. Materials Today Chemistry. 2023, 27, 101351.

27. Renaud; A., Jouan; P. Y., Dumait; N., Girard; S.A., Barreau; N., Uchikoshi; T., Grasset; F., Jobic; S., Cordier ; S., Evidence of the Ambipolar Behavior of Mo(6) Cluster Iodides in All-Inorganic Solar Cells: A New Example of Nanoarchitectonic Concept. ACS Appl. Mater. Interfaces, 2022, 14, 1347–1354.

28. Lladó; E.A., Tabernig; A.S., Veeken; T., Garnett; E. C., Polman; A., Ehrler; B., Photovoltaics Reaching for the Shockley–Queisser Limit. ACS Energy Lett. 2020, 5, 3029–3033.

29. Kirakci; K., Nguyen; T.K.N., Grasset; F., Uchikoshi; T., Zelenka; J., Kubát; P., Ruml; T., Lang; K., Electrophoretically Deposited Layers of Octahedral Molybdenum Cluster Complexes: A Promising Coating for Mitigation of Pathogenic Bacterial Biofilms under Blue Light. ACS Appl. Mater. Interfaces, 2020, 12, 52492–52499.

30. Kirakci; K., Cordier; S., Perrin; C., Synthesis and Characterization of Cs2Mo6X14 (X = Br or I) Hexamolybdenum Cluster Halides: Efficient Mo6 Cluster Precursors For Solution Chemistry Syntheses. Z. Anorg. Allg. Chem., 2005, 63, 411-416.

31. Sharif; N.F.M., Shafie; S., Kadir; M.Z.A. Ab., Hasan; W.Z. W., Mustafa; M.N., Samaila; B., The effect of titanium (IV) chloride surface treatment to enhance charge transport and performance of dye-sensitized solar cell. Results in Physics, 2019, 15, 102725.

32. Pomrnerehne; J., Vestweber; H., Gun; W., Muhrt; R.E., Bassler; H., Porsch; M., Daub; J., Efficient Two Layer LEDs on a Polymer Blend Basis. Adv. Mater., 1995, 7, 551-554.

33. Vorotnikova; Y.A., Efremovab' O.A., Novozhilova; I.N.,Yansholec; V.V., Kuratieva; N.V., Brylev; K.A., Kitamura; N., Mironov; Y.V., Shestopalov; M.I., Hexaazide octahedral molybdenum cluster complexes: Synthesis, properties and the evidence of hydrolysis. Journal of Molecular Structure, 2017, 1134, 237-243.

34. White; R.T.; Thibau; E.S., Lu; Z.H., Interface Structure of MoO_3 on Organic Semiconductors. Sci. Rep., 2016, 6, 21109.

35. Kumari; L., Ma; Y.R., Tsai; C.C., Lin; Y.W., Wu; S.Y., Cheng; K.W., Liou; Y., X-ray diffraction and Raman scattering studies on large-area array and nanobranched structure of 1D MoO2 nanorods. Nanotechnology; 2007, 18, 115717.

36. Mabrouk; K.B., Kauffmann; T.H., Aroui;H., Fontana; M.D., Raman study of cation effect on sulfate vibration modes in solid state and aqueous solutions. J. Raman Spectroscopy, 2013, 44, 1603-1608.

37. Choi; J., Ahn; D.S., Fujitsuka; M., Tojo; S., Ihee; H., Majima; T. Formation of the Charge-

Localized Dimer Radical Cation of 2-Ethyl-9,10-dimethoxyanthracene in Solution Phase. Chem. Eur. J., 2019, 25, 5586 – 5594.

38. Šetka; M., Calavia; R., Vojkůvka; L., Llobet; E., Drbohlavová; J., Vallejos; S., Raman and XPS studies of ammonia sensitive polypyrrole nanorods and nanoparticles. Sci. Rep., 2019, 9, 8465.

39. Virgilio; M.D., Peressut; A.B., Latorrata; S., Mariani; M., Dotelli; G., Graphene oxide-naphthalene sulfonate blends as possible proton exchange membranes. Solid State Ionics, 2022, 376, 115858.

40. Kabiri; K., Zohuriaan-Mehr; M. J., Mirzadeh; H., Kheirabadi; M., Solvent-, ion- and pH-specific swelling of poly(2-acrylamido2-methylpropane sulfonic acid) super absorbing gels, J. Polym. Res., 2010, 17, 203–212.

41. Funaki; T., Otsuka; K., Onozawa-Komatsuzaki; N., Kasuga; K., Sayamaab; K., Sugihara; H., Systematic evaluation of HOMO energy levels for efficient dye regeneration in dye-sensitized solar cells. J. Mater. Chem. A, 2014, 2, 5945-15951.

42. Zhang; T.T., Jia; J.F., Wu; H.S., Substituent and Solvent Effects on Electronic Structure and Spectral Property of ReCl(CO)3(NΛN) (NΛN = Glyoxime): DFT and TDDFT Theoretical Studies. J. Phys. Chem. A , 2010, 114,12251–12257.

43. Chataigner; I., Panel; C., Gérard; H., Piettre; S.R., Sulfonyl vs. carbonyl group: which is the more electron-withdrawing? Chem. Commun., 2007, 31, 288-3290.

44. Bledowski; M., Wang;L., Ramakrishnan; A., Khavryuchenko; O.V., Khavryuchenko; V.D., Ricci; P.C., Strunk; J., Cremer; T., Kolbeckf; C., Beranek; R., Visible-light photocurrent response of TiO2–polyheptazine hybrids: evidence for interfacial charge-transfer absorption, Phys. Chem. Chem. Phys, , 2011, 13, 21511-21519.

45. Xu; Y., Gao; C., Tang; S., Zhang; J., Chen; Y., Zhu; Y., Hu; Z., Comprehensive understanding of TiCl4 treatment on the compact TiO2 layer in planar perovskite solar cells with efficiencies over 20%. J. Alloys and Compounds, 2019, 787, 1082-1088.

46. Sun; H., Xu; Z.T., Zhang; D., First-principles calculations to investigate doping effects on electrical conductivity and interfacial contact resistance of TiO2. Applied Surface Science, 2023, 614, 156202.

47. Cheng; H., Feng; Y., Fu; Z., Zheng; Y., Shao; Y., Bai; Y., Understanding and minimizing non-radiative recombination losses in perovskite light-emitting diodes. J. Mater. Chem. C, 2022, 10, 13590-13610.

48. Shalini; S., Balasundaraprabhu; R., Kumar; T. S., Prabavathy; N., Senthilarasu; S., Prasanna; S. Status and outlook of sensitizers/dyes used in dye sensitized solar cells (DSSC): a review. International Journal of Energy Research, 2016, 40, 1303-1320

49. Supur; M., Fukuzumi; S., Tuning the photo-driven electron transport within the columnar perylenediimide stacks by changing the π-extent of the electron donors. Phys. Chem. Chem. Phys., 2013, 15, 2539-2546.

50. Mikhailov; M. A., Brylev; K.A., Abramov; P.A., Sakuda; E., Akagi; S., Ito; A., Kitamura; N., Sokolov; M. N., Synthetic Tuning of Redox, Spectroscopic, and Photophysical Properties of {Mo6I8}Carboxylate Ligands. Inorg. Chem., 2016, 55, 8437−8445.

51. Hung; C.M., Lin; J.T., Yang; Y.H., Liu; Y.C., Gu; M.W., Chou; T.C., Wang; S.F., Chen; Z.Q., Wu; C.C., Chen; L.C., Hsu; C.C., Chen; C.H., Chiu; C.W., Chen; H.C., Chou; P.T., Modulation of Perovskite Grain Boundaries by Electron Donor–Acceptor Zwitterions R,R-Diphenylamino-phenyl-pyridinium-(CH2)n-sulfonates: All-Round Improvement on the Solar Cell Performance., J. ACS Au , 2022, 2, 1189–1199.

52. Wang; K.L., Lu; H., Li; M., Chen; C.H., Zhang; D.B., Chen; J., Wu; J.J., Zhou; Y.H., Wang; X.Q., Su; Z. H., Shi; Y.R., Tian; Q.S., Ni; Y.Z., Gao; X. Y., Zakeeruddin; S.M., Grätzel; M., Wang; Z.K., Liao; L.S., Ion–Dipole Interaction Enabling Highly Efficient CsPbI3 Perovskite Indoor Photovoltaics., Adv. Mater., 2023, 35, 2210106.

53. Rinke, Hofmann; O.T., Patrick, Band Bending Engineering at Organic/Inorganic Interfaces Using Organic Self-Assembled Monolayers. Adv. Electron.Mater., 2017, 3, 1600373.

54. Schukraft; G.E.M, Moss; B., Kafizas; A.G., Petit; C., Effect of Band Bending in Photoactive MOF-Based Heterojunctions. ACS Appl. Mater. Interfaces, 2022, 14, 19342–19352.

55. Listorti; A., O'Regan; B., Durrant; J. R., Electron Transfer Dynamics in Dye-Sensitized Solar Cells, Chem. Mater., 2011, 23, 3381–3399.

56. Wang; Q., Moser; J.E., Grätzel' M., Electrochemical Impedance Spectroscopic Analysis of Dye-Sensitized Solar Cells. J. Phys. Chem. B, 2005, 109, 14945–14953.

57. Kim; S.G., Ju; M.J., Choi; I.T., Choi; W.S., Choi; H. J., Baek; J.B., Kim; H.K., Nb-doped TiO2 nanoparticles for organicdye-sensitized solar cells. RSC Adv., 2013, 3, 16380–16386.

58. Zaine; S.N.A., Mohamed; N.M., Khatani; M., Samsudin; A.E., Shahid; M.U., Trap State and Charge Recombination in Nanocrystalline Passivized Conductive and Photoelectrode Interface of Dye-Sensitized Solar Cell. Coatings, 2020, 10, 284.

59. Nissfolk; S., Fredin; K., Hagfeldt; A., Boschloo; G., Recombination and Transport Processes in Dye-Sensitized Solar Cells Investigated under Working Conditions. J. Phys. Chem. B, 2006, 110, 17715–17718.

60. Van de Lagemaat; T.J., Park; N.G., Frank; A. J. Influence of Electrical Potential Distribution, Charge Transport, and Recombination on the Photopotential and Photocurrent Conversion Efficiency of Dye-Sensitized Nanocrystalline TiO_2 Solar Cells: A Study by Electrical Impedance and Optical Modulation, J. Phys. Chem. B, 2000, 104, 2044–2052.